RESEARCH ARTICLE

# The role of the fiber–matrix interface in the tensile properties of short fiber–reinforced 3D-printed polylactic acid composites

Csenge Tóth[1,2] | Norbert László Lukács[1] | Norbert Krisztián Kovács[1,2]

[1]Department of Polymer Engineering, Faculty of Mechanical Engineering, Budapest University of Technology and Economics, Budapest, Hungary

[2]MTA-BME Lendület Lightweight Polymer Composites Research Group, Budapest, Hungary

**Correspondence**
Norbert Krisztián Kovács, Department of Polymer Engineering, Faculty of Mechanical Engineering, Budapest University of Technology and Economics, Műegyetem rkp. 3., Budapest H-1111, Hungary.
Email: kovacsn@pt.bme.hu

**Abstract**

In this study, we investigate the relationship between structure and properties of fiber–matrix adhesion for material extrusion–based 3-dimensional (3D) printed composites. We examine the influence of fiber length and fiber content on the tensile properties of glass, basalt, and carbon fiber–reinforced polylactic acid (PLA) composites. Short fiber–reinforced filaments were produced, then, simple micromechanical models were used to predict the in-plane tensile properties. We found that interlayer tensile properties are strongly influenced by fiber–matrix adhesion. If adhesion is sufficient, the fibers and matrix deform together under tensile load. A second-order relationship describes interlayer tensile strength in relation to fiber content between 5 and 25 w%, with a maximum at 15 w%, for carbon and basalt fiber–reinforced composites. If adhesion is weak, the crack propagates along the fiber–matrix interface, causing brittle fracture and low strength. This behavior was noted for the glass fiber composite, for which the calculated interface shear strength was the lowest (1.4 MPa). In this case, fiber content is inversely proportional to interlayer tensile strength. Our results show the role of fiber–matrix adhesion quality on tensile properties, which has a major impact on both the accuracy of predictions and the damage processes.

**Highlights**

- Critical fiber length determines accuracy of tensile property estimates
- Quality of fiber–matrix adhesion governs interlayer damage process
- Poor adhesion causes brittle fracture and low strength
- Second-order relationship of interlayer tensile strength and fiber content
- Loss of interlayer tensile strength in composite due to fiber–matrix interface

**KEYWORDS**

additive manufacturing, analytical modeling, fiber-matrix adhesion, filament, polymer composite

# 1 | INTRODUCTION

Research on 3D-printed composites is widespread but there are still areas that need investigating. Material extrusion 3D printing is well-suited for the processing of short fiber–reinforced thermoplastic composites, therefore it is widely used for industrial and research purposes. The fibers are mostly used to improve mechanical properties such as tensile[1,2] and flexural properties,[3–5] and dynamic[6,7] behavior. By combining short fibers with nanoparticles, functional properties such as electrical or thermal conductivity, or shape memory can be achieved.[8–10] Despite intensive research in this area, methods for estimating mechanical properties are still underdeveloped. The macroscale properties of 3D-printed composites are greatly affected by fiber length, orientation, fiber–matrix adhesion and void content, so these should be incorporated into predictive calculations. However, microstructural features depend on the manufacturing process, and thus have little predictability in the product.[11] The mechanical, thermal, wear, etc. properties of the polymers used for 3D printing are also very diverse, which can cause further difficulties.[12] Overall, the effects of manufacturing parameters on mechanical properties ranges widely and is difficult to generalize.[13] Accurate modeling also requires sufficient quantitative data, which can be time-consuming and error-prone to collect. Polyzos et al.[14] aimed to overcome the time-consuming data processing for micromechanical modeling with a stochastic approach. The authors generated artificial fibers and presented a semi-analytical modeling method to estimate elastic properties. The stochastic modeling could give comparable predictions to deterministic modeling (where fiber properties are extracted from X-ray microtomography images), and it reduced pre-processing time significantly.

But most often, microstructural features are determined experimentally. Nasirov et al.[15] presented three-scale homogenization from bead level to macroscale level for carbon fiber–reinforced polylactic acid composites. The authors showed that fiber orientation and fiber length distribution should be measured to improve accuracy. Gupta et al.[16] applied the Mori-Tanaka approach with a two-step homogenization framework to predict Young's modulus and tensile strength in relation to fiber content. For homogenization, they considered and determined fiber length and bead size (the diameter of a single 3D-printed extrudate) experimentally. They found that the method reduces the error mostly for higher fiber contents, in the case of carbon fiber–reinforced polycarbonate composites. Abderrafai et al.[17] also presented homogenization based on the Mori-Tanaka model to predict the Young's modulus of carbon fiber–reinforced polyamide composites. The authors showed that their method provides a lower bound for mechanical properties and that experimental values below this bound indicate imperfect fiber–matrix adhesion. Sufficient fiber–matrix adhesion is key to efficient load transfer.[18] Yu et al.[19] showed that fiber–matrix adhesion strongly affects the properties of 3D-printed composites, not only in terms of strength but also in terms of ductility. The authors conducted in-situ X-ray tomography during tensile testing and found that the composites had several components in a hierarchical structure and distinctive fracture behavior, in which voids have a key role. Yilmaz et al.[20] have shown that post-processing can successfully eliminate most of the voids, which can result in an increase in mechanical properties. Pei et al.[11] applied the Halpin-Tsai model with parameter adjustment, where fiber and void volume fractions were considered as stochastic variables. They also analyzed the effects of process parameters on the structure. The authors revealed a structure–property relationship between void distribution and Young's modulus. The Classical Laminate Theory (CLT) is also often used to estimate macro-level properties of 3D-printed composites, but mostly for composites reinforced with continuous fibers.[21]

The studies listed above investigated mechanical properties along the length of the part. 3D-printed structures are anisotropic, which means that there can be a large difference (even an order of magnitude) between in-plane mechanical properties and mechanical properties perpendicular to the printing direction. König et al.[22] investigated the effects of process parameters on the interlayer bonding of carbon fiber–reinforced polyamide composites. The authors found that the carbon fibers decrease interlayer bonding strength, probably due to weak fiber–matrix adhesion. Bhandari et al.[23] found that carbon fibers reduce the interlayer tensile strength by 66% and 50% for an amorphous and a semi-crystalline polymer, respectively. Post-processing increases strength but also increases production time and can deform 3D-printed products. The authors reported that increased melt viscosity and crystallization inhibit diffusion between layers and can therefore result in poor interlayer bond strength.

Overall, further research is needed to explore the complex microstructure and process–structure relationships of 3D-printed composites. Most studies are concerned with longitudinal (in-plane) mechanical properties, the load response in other orientations is less explored. In this study, we examine the impacts of fiber length, fiber content, and fiber–matrix adhesion on the tensile properties of glass, basalt, and carbon

fiber polylactic acid (PLA) composites. Tensile properties were determined from both in-plane and interlayer tests. We also present predictions of tensile strength and Young's modulus based on the Rule of Mixtures and the Halpin-Tsai model. Our results provide a better insight into the role of interfaces in 3D-printed composites and help to develop more accurate predictive models.

## 2 | MATERIALS AND METHODS

### 2.1 | Preparation of the composite filaments

We used Ingeo 4060D polylactic acid (PLA) from Natureworks LLC. (USA) as the matrix of the composites. The density of PLA is 1.24 g/cm$^3$. Chopped carbon fibers (PX35) were obtained from Zoltek Corporation (USA). According to the supplier, the fibers have an epoxy surface treatment. Chopped basalt fibers (KV-18) were obtained from Kamenny Vek (Russia). The fibers were cut from a continuous yarn and sized for compounds based on polypropylene and polyethylene. As basalt is natural, PLA composites reinforced with basalt fibers have the potential to be a more sustainable thermoplastic composite alternative for semi-industrial

applications.[24,25] Table 1 shows the material properties of the fibers and the matrix (4060D PLA). The fiber length and diameter presented in Table 1 are used as a reference for interpreting the fiber length results presented in later chapters. The density and mechanical properties of the constituents were used to calculate the mechanical properties of the composites. The PLA pellets were dried for 4 h at 45°C before processing in a WGLL-125 BE drying oven from Faithful Instrument Co., LTD (China).

Figure 1 illustrates the manufacturing process of the composite filaments, and Table 2 summarizes the main process parameters. First, the dry mixtures were prepared in the appropriate weight ratios (5, 10, 15, 20, 25 w%). Then the mixtures were fed to a twin-screw extruder (LTE 26–44 manufactured by Labtech Engineering Co., Ltd., Thailand). The screw diameter and the L/D ratio were 26 mm and 44, respectively. The zone temperatures from hopper to die were 180, 190, 190, 190, 190, 200, 200, 200, 200, 200, and 190°C in all cases. Compounding is a very important step to make composite filaments processable with 3D printing. Homogeneous distribution of the reinforcing fibers must be ensured, otherwise, clumps of fibers can clog the nozzle. However, during compounding, the fibers are subjected to significant shear stress, which causes breakage.[31] We aimed to minimize fiber breakage to achieve the longest possible residual

**TABLE 1** Material properties of the matrix and the fibers used as reinforcements.[26–30]

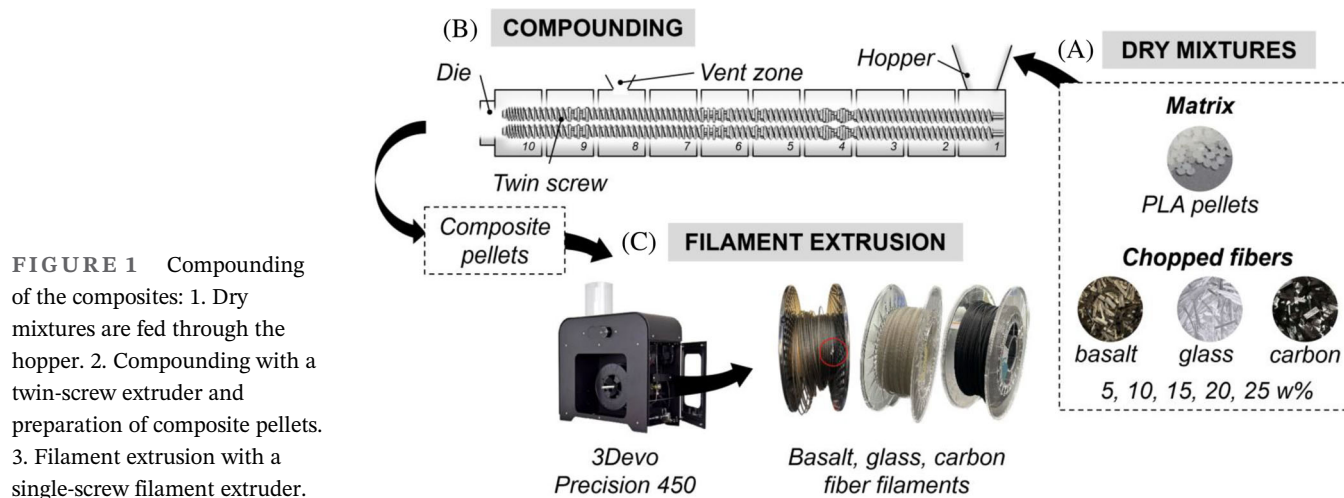| Material type | Fiber length (mm) | Fiber diameter (μm) | Density (g/cm$^3$) | Tensile strength (MPa) | Young's modulus (GPa) |
|---|---|---|---|---|---|
| 4060D PLA | - | - | 1.24 | 55 | 3 |
| Carbon fiber | 8 | 7 | 1.37 | 4137 | 242 |
| Basalt fiber | 10 | 12 | 2.59 | 2335 | 85 |
| Glass fiber | 8 | 14 | 2.55 | 1956 | 78 |



**FIGURE 1** Compounding of the composites: 1. Dry mixtures are fed through the hopper. 2. Compounding with a twin-screw extruder and preparation of composite pellets. 3. Filament extrusion with a single-screw filament extruder.

fiber length. Therefore, we investigated the influence of screw speed on fiber fracture. Composites were produced with screw speeds of 40, 60, 80, and 120 1/min, and residual fiber length was measured. The tests were carried out with a composite containing a PLA matrix and 10 w% carbon fiber.

The number average fiber length ($L_n$) decreased linearly as a function of screw speed. At 40 1/min $L_n = 220 \pm$ µm while above 80 1/min, the length average reduced below 200 µm, which means that the proportion of long fibers was significantly reduced. We were looking for an optimum speed that would minimize breakage while keeping the manufacturing process productive, so we produced the composites at 60 1/min. After compounding, the composite extrudates were cut into 6 mm long pellets with a LZ-120/VS granulator from Labtech Engineering Co., Ltd. (Thailand). We then fed the pellets to a single-screw filament extruder (Precision 450, 3devo Inc., The Netherlands) to prepare the filaments for 3D printing. Screw speed (r) was 4.5 rpm and the zone temperatures from hopper to die were 170, 210, 185, and 175°C. Filament diameter was $1.7 \pm 0.5$ mm. Neat PLA filaments were also produced with the same process to ensure the same manufacturing history of the materials.

We produced two types of specimens for tensile testing. To measure in-plane tensile properties, we used the 5A-type geometry described in ISO 527-2:2012 (Figure 2A). The specimens were laid flat on the print bed and the printing orientation was parallel to the longitudinal axis (0°) in each layer. To measure the interlayer

tensile properties, we designed a custom specimen (Figure 2B). Hollow boxes with one contour were prepared, then the rectangle specimens for testing were cut with lever plate shears. Wall thickness was 0.8 mm. The tests were performed with the direction of the load perpendicular to the direction of building so that the interlayer properties could be measured. The 25 w% basalt fiber–reinforced filament could not be used for box specimens due to the brittleness of the filament.

All specimens were produced on a Prusa Mini desktop 3D printer (Prusa Research, Czech Republic). To generate the G-codes we used the Ultimaker Cura 4.13.1 software (Ultimaker B.V., The Netherlands). The diameter and the temperature of the nozzle were 0.8 mm and 200°C, respectively. Layer height was 0.2 mm, and the infill rate was 100%. The print bed was heated to 60°C and no fan cooling was used.

## 2.2 | Microstructural analysis

We measured the average fiber length for each composite after processing. We cut samples of 2–3 g, then we burned the PLA at 600°C for 4 h in a Denkal 6B furnace (Kalória Hőtechnikai Kft., Hungary). The remaining fibers were dispersed on glass sheets, and the individual lengths were measured with the use of a Keyence VHX-5000 (Keyence Corporation, Belgium) digital microscope at 40× magnification. At least 200 fibers were measured in all cases. The number averages and the length-

**TABLE 2** Filament production process steps and their main manufacturing parameters.

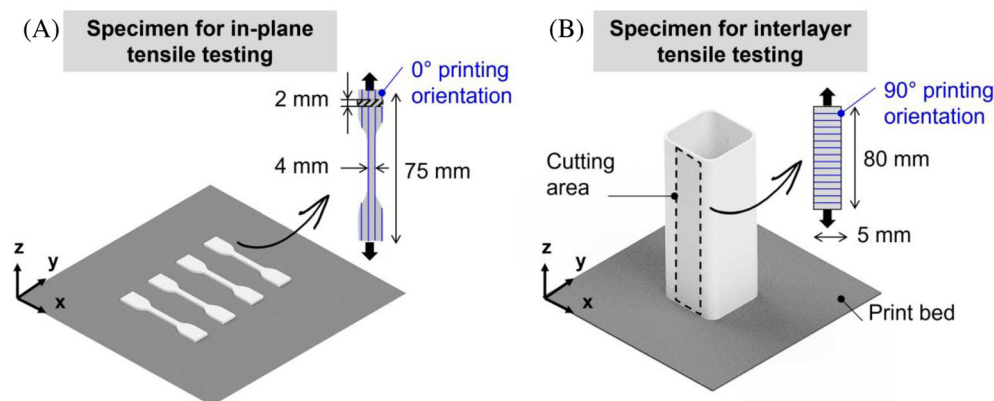| No. | Procedure | Temperature profile from hopper to die (*if applicable*) | Speed (1/min) |
|---|---|---|---|
| 1 | Dry mixing | Room temperature | Hand mixing/not applicable |
| 2 | Compounding | 180–190–200–190°C | 60 |
| 3 | Granulation | Room temperature | 40 |
| 4 | Filament extrusion | 170–210–185–175°C | 4.5 |



**FIGURE 2** Specimens (A) for in-plane tensile testing (0° printing orientation) and (B) for interlayer tensile testing (90° printing orientation).

weighted averages were calculated with Equations (1) and (2), respectively. The probability density function of the Weibull distribution is given by Equation (3).[32]

$$L_n = \frac{\sum n_i L_i}{\sum n_i} \qquad (1)$$

$$L_w = \frac{\sum n_i L_i^2}{\sum n_i L_i} \qquad (2)$$

where $L_i$ (μm) is the length of fiber $i$, $n_i$ is the number of fibers of length $L_i$ and $n$ is the number of fibers.

$$f(l|a,b) = \frac{b}{a}\left(\frac{x}{a}\right)^{b-1} e^{-\left(\frac{x}{a}\right)^b} \; if \; x \geq 0 \qquad (3)$$

where $a$ and $b$ are the scale and the shape parameters, respectively.

We determined the critical fiber length ($L_{crit,est}$) using Equation (4), which is an estimation based on the average fiber ($L_n$).[33] Critical fiber length was also calculated from the measured tensile strengths for comparison (based on Equation 7). Then, interfacial shear strength was calculated with Equation (4) for each composite.[32]

$$L_{crit,est} = \frac{4}{3}L_n \qquad (4)$$

$$L_{crit,calc} = \frac{\sigma_f d_f}{2\tau} \qquad (5)$$

where $L_n$ (mm) is the number average fiber length, $\tau$ (MPa) is interfacial shear strength at the fiber–matrix interface, $\sigma_f$ (MPa) is the ultimate tensile strength of a single fiber and $d_f$ (mm) is fiber diameter.

We analyzed the broken surfaces of the specimens after tensile testing using a Keyence VHX-5000 (Keyence Corporation, Belgium) digital microscope, and a JSM 6380LA scanning electron microscope from Jeol Ltd. (Japan). For scanning electron microscopy, the samples were sputtered with gold.

## 2.3 | Tensile properties

In-plane and the interlayer tensile properties were determined with a Zwick Z005 (Zwick Roell AG, Germany) universal testing machine in accordance with the ISO 527 standard, with a cross-head speed of 5 mm/min, at 25°C and in 20% relative humidity. 20 kN-rated Zwick 8131 screw grips were used. Gripping distance was 50 mm for both types of specimens. We tested 5 specimens in each case. Young's modulus was determined as a chord slope between 0.05% and 0.25% strains.

## 2.4 | Micromechanical models

We applied simple micromechanical models to estimate the in-lane tensile properties. The models consider the impact of fiber length in different ways, for which a correction factor is introduced ($\chi_L$). In the simplest case, we used the Rule of Mixtures (Equation 6) and fiber length was not taken into account ($\chi_L = 1$). In the Halpin-Tsai model (Equation 7), the fiber length correction factor depends on the number average fiber length, and critical fiber length (Equation 8). The number average fiber lengths and the fiber length distributions were determined experimentally. We estimated the critical fiber lengths ($L_{crit}$) for all composites with Equation (4). Then, we calculated the tensile strengths with the Halpin-Tsai model, where the fiber length correction factors were determined with the use of measured fiber length data. The elastic moduli were estimated based on the same principle. The Rule of Mixtures (Equation 6) was applied in the simplest case, and fiber length was taken into account in the Halpin-Tsai method (Equation 7). Fiber orientation also affects mechanical properties, but it has been shown that in 3D-printed composites orientation usually aligns with the printing direction.[34,35] In this study, we prepared unidirectional composites therefore we did not consider the effects of orientation in the calculations.

$$X_{ROM} = X_f v_f + v_m X_m \qquad (6)$$

$$X_{HT} = \chi_L X_f v_f + v_m X_m \qquad (7)$$

where $X$ stands for tensile strength or Young's modulus and $v$ is fiber volume fraction. The subscripts 'f' and 'm' stand for fiber and matrix, respectively, and $\chi_L$ is the fiber length correction factor. The tensile strength and Young's modulus values used for the calculations are given in Table 1. The fiber volume fraction is given by Equation (8):

$$v_f = \frac{\frac{w_f}{\rho_f}}{\frac{w_f}{\rho_f} + \frac{w_m}{\rho_m}} \qquad (8)$$

where $w$ (g) is the weight and $\rho$ (g/cm³) is the density. The subscripts 'f' and 'm' stand for fiber and matrix, respectively. The densities were given in Table 1.

$$\chi_L = \int_{L_{min}}^{L_{crit,est}} \left[ l^2 / (2L_{crit,est} L_n) \right] f(l) dl$$

$$+ \int_{L_{crit,est}}^{L_{max}} \left(\frac{l}{L_n}\right) \left[ 1 - \frac{L_{crit,est}}{2l} \right] f(l) dl \qquad (9)$$

where $L_n$ (mm) is the number average fiber length, $L_{crit,est}$ (mm) is the estimated critical fiber length, $L_{min}$ and $L_{max}$ (mm) are the shortest and the longest fibers measured, respectively, and $f(l)$ is the fiber length distribution function.

The accuracy of the estimates is characterized by relative error (Equation 10)

$$\delta\,(\%) = \left| \frac{X_{measured} - X_{calc}}{X_{measured}} \right| \times 100 \qquad (10)$$

where $X$ stands for tensile strength or Young's modulus and the subscripts 'measured' and 'calc' stand for the measured properties and the estimated values, respectively.

## 3 | RESULTS AND DISCUSSION

### 3.1 | Fiber length distribution

We fitted the Weibull distribution function on all the fiber length results (Figure 3). These distributions were used to obtain the fiber length correction factors (Equation 9). Generally, the distributions shifted towards shorter lengths as fiber content increased. We calculated

the horizontal displacement of the peak maximum between the lowest and the highest fiber contents. The peak shift was 139 μm, 84 μm and 209 μm for the glass, basalt and carbon fibers, respectively. This shows that the impact of fiber content on fiber length was most prominent for carbon fiber-reinforced composites, while the basalt fiber-reinforced composites were least affected. Figure 3D shows the number averages and the length-weighted averages. The longest remaining fiber length was achieved for the glass fiber composites ($\overline{L_n} = 642 \pm 62\,\mu m$), while the shortest were the basalt fibers ($\overline{L_n} = 246 \pm 42\,\mu m$). The slope of the lines fitted to the data points decreases monotonically, with the steepest slope for carbon fibers. This shows that carbon fibers fragment the most with increasing fiber content.

In the literature, average fiber length is between 100 and 500 μm,[36–39] but very short fiber lengths of less than 100 μm can also be found.[15] By comparison, it is common to produce products with an average fiber length of more than 1 mm with other thermoplastic composite manufacturing techniques that is, injection molding or compression molding.[40,41] Producing long fiber–composites with material extrusion 3D printing is not yet common due to technological limitations. In the case of a desktop 3D printer, the print head is usually equipped with nozzles with a
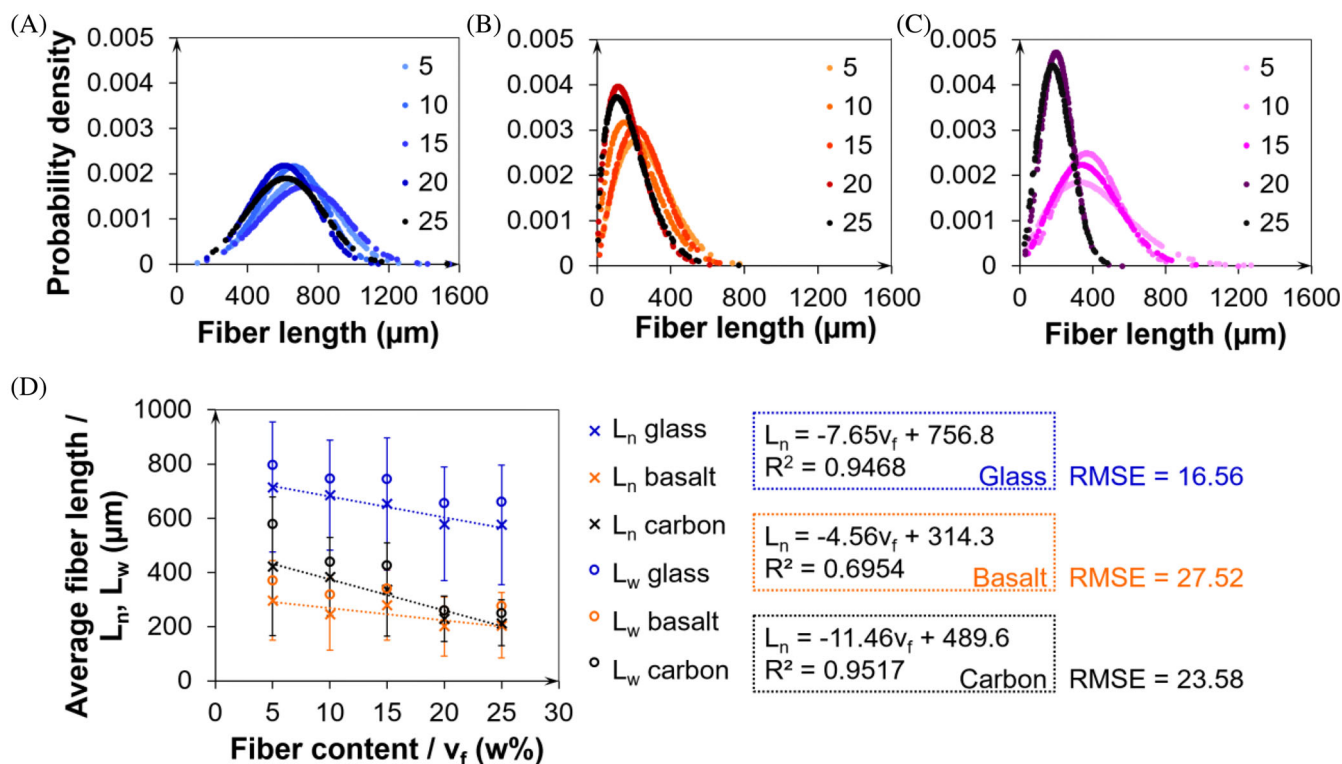


**FIGURE 3** Fiber length distributions of the (A) glass, (B) basalt, and (C) carbon fiber–reinforced composites, and (D) the average fiber lengths (number and length-weighted).

narrow orifice (with a diameter of 0.1–1 mm), which is prone to clogging. Zhang et al.[42] found that nozzle clogging is less dependent on the viscosity of the matrix and more on fiber volume fraction and fiber length.

## 3.2 | In-plane tensile properties

Figure 4 shows experimental in-plane tensile strength and Young's modulus, and the results of the estimations based on the Rule of Mixtures (RoM) and the Halpin-Tsai (HT) method. The results are presented in Table 3. The estimates were calculated for discrete fiber contents, and a linear trend was fitted to each (Equation 11). A linear trend was also fitted to the experimental results. A linear relationship is expected based on the RoM, but for short-fiber composites, the length correction factor can have a large effect on the type of relationship. However, a linear relationship was found between average fiber length and fiber content, with a relatively small decreasing slope (Figure 3). Therefore, if the length is not significantly impacted by fiber content, tensile strength and Young's modulus can be estimated with a linear relationship. The nature of the relationship is not affected by fiber length, only by its slope. This can be observed for glass and basalt fiber–reinforced composites. However, for the carbon fiber composites, tensile strength was below the estimated value for the higher fiber content (25%). The length of the carbon fibers was most dependent on fiber content, thus these results support our findings.

$$X_{composite}(MPa) = av_f + X_{matrix} \qquad (11)$$

where $X$ stands for tensile strength ($\sigma$) or Young's modulus ($E$), $a$ is the slope and $v_f$ is fiber weight content. $\sigma_{matrix} = 60$ MPa is the measured tensile strength and $E_{matrix} = 3.1$ GPa is the measured modulus of the neat PLA.

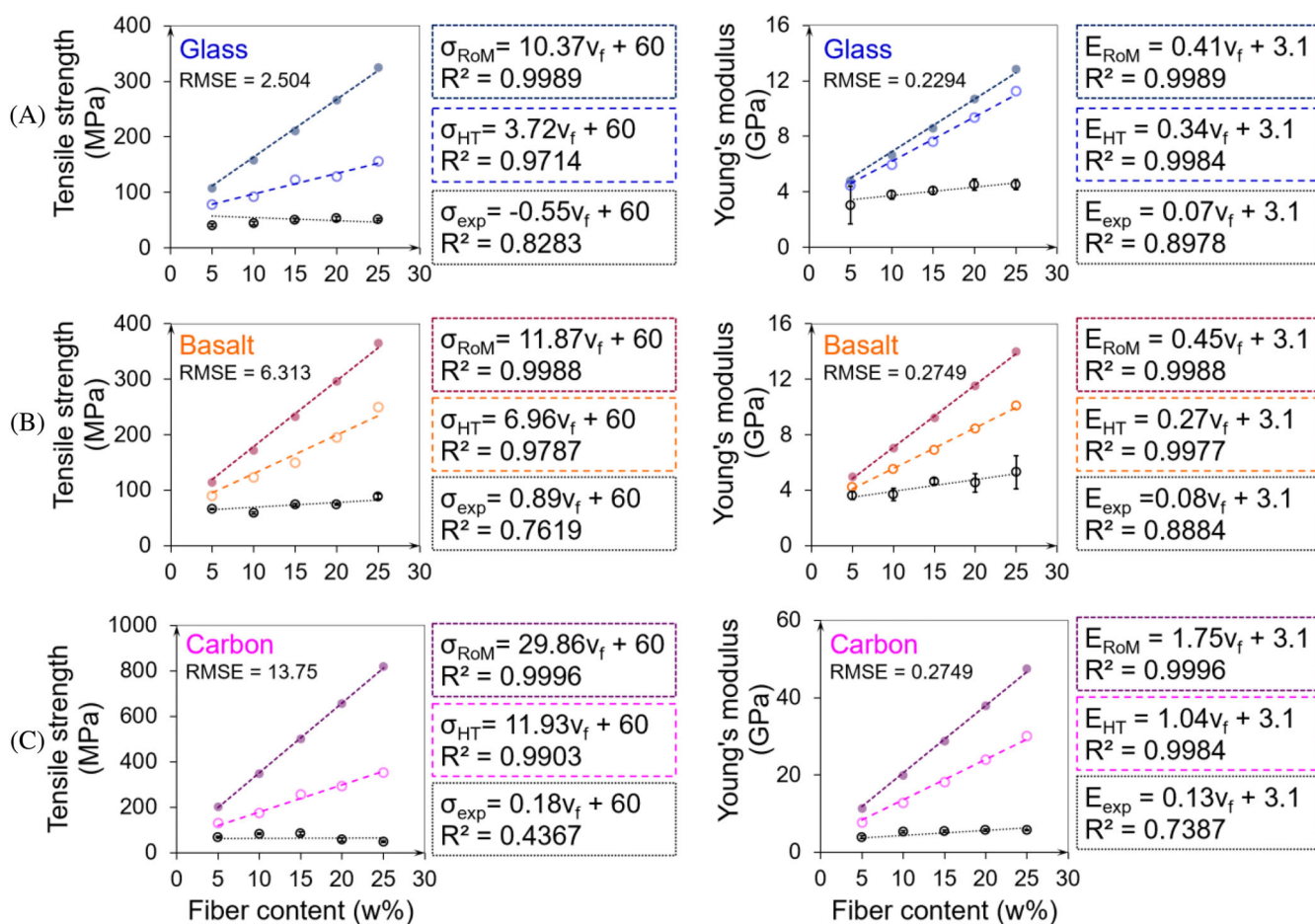The predictions based on the RoM overestimate tensile strength and Young's modulus by orders of



**FIGURE 4** In-plane tensile strength and Young's modulus of the (A) glass, (B) basalt, and (C) carbon fiber composites as a function of fiber content. RMSE values refer to the linear fits of the measured tensile strength ($\sigma_{exp}$) and Young's modulus ($E_{exp}$).

**TABLE 3** Experimental results (average strength and standard deviation) and predicted in-plane tensile strength and Young's modulus.

| Type | Fiber content $v_f$ (w%) | Measured in-plane tensile strength $\sigma_{exp}$ (MPa) | Predicted in-plane tensile strength | | Measured in-plane Young's modulus $E_{exp}$ (GPa) | Predicted in-plane Young's modulus | |
|---|---|---|---|---|---|---|---|
| | | | $\sigma_{HT}$ (MPa) | $\sigma_{RoM}$ (MPa) | | $E_{HT}$ (GPa) | $E_{RoM}$ (GPa) |
| 4060D PLA | 0 | 56.7 ± 7.3 | - | - | 3.10 ± 0.4 | - | - |
| Glass | 5 | 40.6 ± 2.6 | 78.1 | 107.5 | 3.02 ± 1.4 | 4.44 | 4.76 |
| | 10 | 44.4 ± 3.0 | 92.2 | 157.6 | 3.78 ± 0.3 | 5.97 | 6.62 |
| | 15 | 50.4 ± 2.9 | 122.1 | 210.6 | 4.09 ± 0.3 | 7.61 | 8.59 |
| | 20 | 53.0 ± 3.3 | 128.2 | 266.7 | 4.52 ± 0.4 | 9.36 | 10.67 |
| | 25 | 51.3 ± 2.1 | 156.0 | 326.1 | 4.52 ± 0.4 | 11.23 | 12.88 |
| Basalt | 5 | 65.4 ± 1.0 | 90.1 | 114.3 | 3.59 ± 0.3 | 4.20 | 4.96 |
| | 10 | 58.6 ± 2.2 | 122.9 | 171.6 | 3.68 ± 0.5 | 5.50 | 7.02 |
| | 15 | 73.7 ± 2.2 | 149.0 | 232.3 | 4.64 ± 0.2 | 6.90 | 9.21 |
| | 20 | 74.4 ± 1.8 | 195.3 | 296.7 | 4.52 ± 0.7 | 8.42 | 11.53 |
| | 25 | 88.5 ± 4.8 | 249.9 | 365.0 | 5.30 ± 1.2 | 10.07 | 13.99 |
| Carbon | 5 | 67.9 ± 4.1 | 129.5 | 201.9 | 3.88 ± 0.4 | 7.72 | 11.32 |
| | 10 | 82.9 ± 4.2 | 175.1 | 348.4 | 5.25 ± 0.3 | 12.76 | 19.91 |
| | 15 | 83.8 ± 7.9 | 255.1 | 499.7 | 5.42 ± 0.2 | 18.13 | 28.78 |
| | 20 | 56.2 ± 7.1 | 292.8 | 656.2 | 5.72 ± 0.2 | 23.88 | 37.95 |
| | 25 | 48.1 ± 4.3 | 353.0 | 817.9 | 5.74 ± 0.2 | 30.06 | 47.43 |

magnitude. As the effect of fiber length is not included in the calculation, it is assumed that the tensile strength of each fiber is fully utilized when subjected to tensile load. However, the degree of fiber utilization is determined by the efficiency of load transfer between the fiber and the matrix. For length-corrected calculations (HT method), the slope of the fitted lines is considerably reduced, but the measured properties are still grossly overestimated. Up to 15 w% fiber content, the relative errors were below 120% for tensile strength. The errors calculated for Young's modulus were below 50% for basalt and glass up to 15% fiber content, while for carbon they were below 50% only at 5% fiber content.

The fiber length correction factor is calculated with the use of experimental fiber length data and it is strongly dependent on critical fiber length ($L_c$). However, $L_c$ is usually estimated and rarely measured, because current test methods are prone to error.[26] Thus, the value of $L_c$ is usually taken from literature data, which can lead to inaccuracy, since critical fiber length depends on fiber–matrix adhesion. The quality of adhesion depends on several aspects, such as compatibility, the surface treatment of the fibers, or the processing conditions, and therefore it is a specific characteristic of the materials used. In other cases, it is derived from the number average fiber length, as described in Chapter 2.3. However, the difference between the estimated and the experimental slopes

show that the critical fiber length derived from the average is not applicable in practice because it does not take into account the quality of fiber–matrix adhesion. From the fitted tensile strengths, we estimated the critical fiber lengths of the composites using Equations (7) and (9). Then, we calculated interfacial shear strength ($\tau$) at the fiber–matrix interface using Equation (5) (Table 4). Compared to the number and the length-weighted averages, there is a difference of an order of magnitude between the measured fiber length and the critical fiber length required for adequate reinforcement. The smallest interfacial shear strength was estimated for the glass fiber composites (1.4 MPa), which is reflected in the flat slope of the fitted tensile strength curve. In the case of the basalt fiber composites, the tensile strength results are similar to those reported in the literature,[43,44] so interfacial shear strength (10.4 MPa) can be considered adequate. Lastly, the interfacial shear strength estimated for the carbon fiber composites (7.2 MPa) is higher than that measured by Li et al. (~2 MPa).[45] However, when compared to the study of Chen et al.[46] in which they investigated injection-molded carbon fiber PLA composites, it can be seen that the reinforcing effect of carbon fibers is far lower than expected. In all the literature references mentioned above, only the class of material is the same (fiber type and PLA), not the exact type, so they are only suitable for a comparison of magnitude.

**TABLE 4** Number average and length-weighted fiber length averages and critical fiber lengths determined with different approximating methods.

| | $\overline{L_n}$ ($\mu m$) | $\overline{L_w}$ ($\mu m$) | $\overline{L_{crit}} = \frac{4}{3L_n}$ ($\mu m$) | $L_{crit,calc}$ ($\mu m$) | $\tau$ (MPa) |
|---|---|---|---|---|---|
| Glass | $642 \pm 62$ | $720 \pm 60$ | $856 \pm 83$ | 10,000 | 1.4 |
| Basalt | $246 \pm 43$ | $313 \pm 44$ | $328 \pm 58$ | 1400 | 10.4 |
| Carbon | $318 \pm 92$ | $390 \pm 14$ | $424 \pm 12$ | 2000 | 7.2 |

**FIGURE 5** Interlayer tensile properties (A) tensile strength, (B) Young's modulus, (C) Elongation at break.
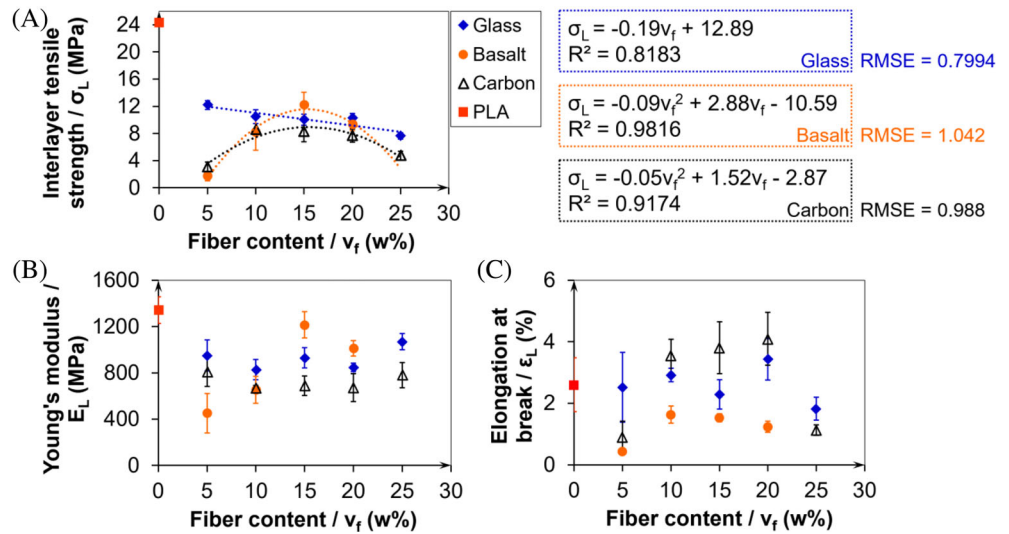


**TABLE 5** Experimental results (average strength and standard deviation) and predicted interlayer tensile strengths.

| Type | Fiber content $v_f$ (w%) | Interlayer tensile strength $\sigma_{exp}$ (MPa) | Young's modulus $E_L$ (MPa) | Elongation at break $\varepsilon_L$ (%) |
|---|---|---|---|---|
| 4060D PLA | 0 | $24.3 \pm 4.4$ | $1342.4 \pm 114.5$ | $2.61 \pm 0.88$ |
| Glass | 5 | $12.2 \pm 0.7$ | $950.4 \pm 134.5$ | $2.52 \pm 1.13$ |
| | 10 | $10.5 \pm 1.0$ | $827.2 \pm 88.0$ | $2.92 \pm 0.22$ |
| | 15 | $10.0 \pm 0.8$ | $929.0 \pm 87.0$ | $2.29 \pm 0.48$ |
| | 20 | $10.3 \pm 0.7$ | $846.7 \pm 36.4$ | $3.43 \pm 0.67$ |
| | 25 | $7.6 \pm 0.5$ | $1069.3 \pm 70.3$ | $1.83 \pm 0.37$ |
| Basalt | 5 | $1.7 \pm 0.7$ | $452.0 \pm 170.3$ | $0.45 \pm 0.09$ |
| | 10 | $8.1 \pm 2.6$ | $652.6 \pm 115.9$ | $1.63 \pm 0.28$ |
| | 15 | $12.2 \pm 1.8$ | $1215.6 \pm 113.1$ | $1.53 \pm 0.13$ |
| | 20 | $9.3 \pm 0.9$ | $1011.4 \pm 66.2$ | $1.24 \pm 0.18$ |
| | 25[a] | N/A | N/A | N/A |
| Carbon | 5 | $3.1 \pm 1.7$ | $809.9 \pm 126.8$ | $0.90 \pm 0.51$ |
| | 10 | $8.5 \pm 0.2$ | $666.4 \pm 23.8$ | $3.54 \pm 0.54$ |
| | 15 | $8.3 \pm 1.5$ | $687.6 \pm 85.0$ | $3.81 \pm 0.84$ |
| | 20 | $7.7 \pm 1.0$ | $672.0 \pm 121.0$ | $4.10 \pm 0.86$ |
| | 25 | $4.7 \pm 0.6$ | $779.4 \pm 109.6$ | $1.13 \pm 0.17$ |

[a]Basalt 25 w% type composite could not be measured due to failed 3D printing.

## 3.3 | Interlayer tensile properties

Figure 5 shows the interlayer tensile properties in relation to fiber content. The results are summarized in Table 5. Overall, interlayer tensile strength was lower than that of the unfilled PLA for all composites. For glass fiber–reinforced PLA, interlayer tensile strength decreased linearly with increasing fiber content between

5 and 25 w%. The equation of the fitted line and the goodness of fit are shown in Figure 5A. For basalt and carbon fiber–reinforced composites, the dependence of interlayer strength on fiber content can be described with a second-order function, with a local maximum at 15 w% in both cases. The fitted second-order polynomials and the accuracy of the fits are shown in Figure 5A. The interlayer Young's modulus of all composites was lower than the modulus of neat PLA. In the case of the glass and carbon fiber–reinforced PLA, no significant effect of fiber content was observed in the 5–25 w% range. The interlayer Young's modulus of the basalt fiber composites reached a local maximum at 15 w%. Lastly, elongation at break increased for carbon fiber composites but decreased when basalt fibers where used, compared to unreinforced PLA. In the case of glass fibers, no change was detectable due to the high scatter.

Figure 6 shows optical microscopy images of the composites with the lowest and highest fiber contents taken after the interlayer tensile tests. For glass fiber–reinforced composites (Figure 6A), the crack penetrated through the layers, indicating that sufficient polymer diffusion occurred. The magnification shows that the surfaces of the protruding glass fibers are completely smooth, which suggests poor fiber-matrix adhesion. This was also confirmed by the SEM image in Figure 7A, which shows a clear separation of the glass fibers from the matrix. In the case of the basalt fiber composite with low fiber content (Figure 6B), the crack ran horizontally between two layers, indicating poor interlayer bonding. Material gaps

in the top layer could be due to deformation during tensile testing. In the case of the 20 w% basalt fiber PLA samples, the crack propagated through the layers. The SEM images of the fracture surface (Figure 7B) show that the basalt fibers separated from the matrix with a clean surface. On the matrix, signs of brittle fracture can be observed. The carbon fiber–reinforced composites showed similar damage modes regardless of fiber content. On the fracture surface, fibers parallel to the load direction can be detected, suggesting that the fibers were bent as the matrix deformed, until they broke. Figure 7C shows that the PLA thinned where the fibers were torn out of the matrix, confirming that the fibers and the matrix have deformed together until failure.

A theoretical sketch of the in-plane and the interlayer failure of 3D-printed short-fiber composites under tensile load is shown in Figure 8. The angle between the fibers and the direction of the load affects the efficiency of reinforcement. When the short-fiber composite is prepared by material extrusion 3D printing, the fibers are mostly aligned with the printing direction.[47,48] Therefore, in the unidirectional composites, the fibers are parallel to the load when subjected to in-plane tensile tests. Under tensile loading, short fiber-reinforced thermoplastic composites generally exhibit the following damage modes: matrix cracking, fiber failure and fiber-matrix failure.[49] In addition, Mészáros et al.[50] found that different matrix fractions (the mobile amorphous, rigid amorphous and crystalline phases) participate in the damage process in different ways. These damage modes are typical when
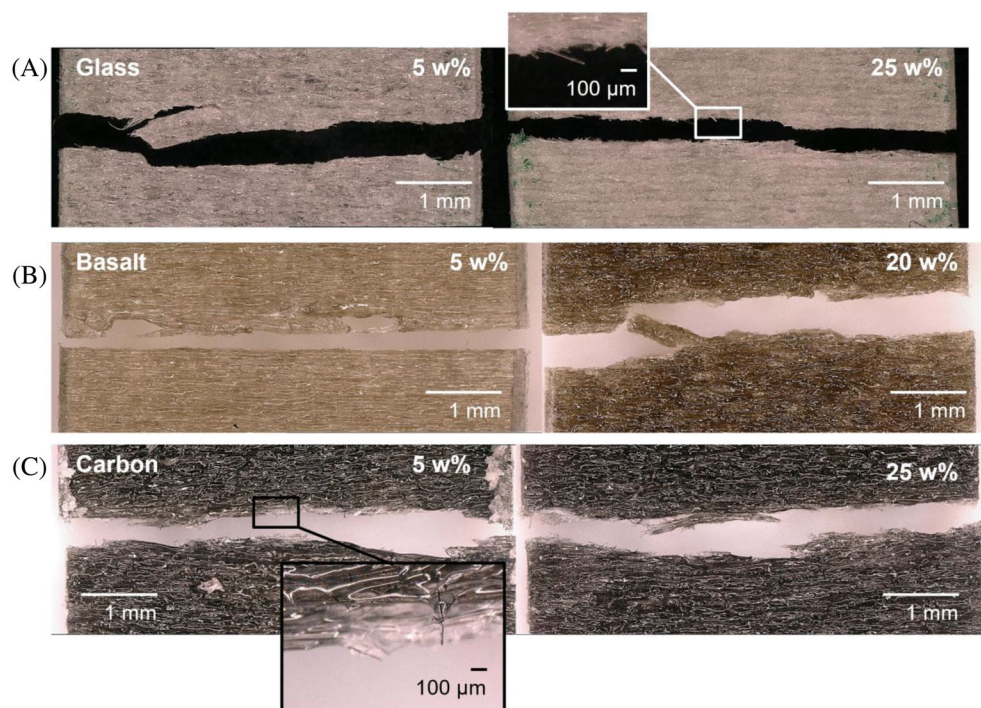


**FIGURE 6** Optical microscope images of the specimens after failure in the case of (A) glass, (B) basalt, and (C) carbon fiber-reinforced composites.

**Fiber-matrix separation**

(A) Clean fiber surface

(B) Fiber imprint surrounded by brittle fractured matrix

(C) Fiber imprint surrounded by ductile deformed matrix
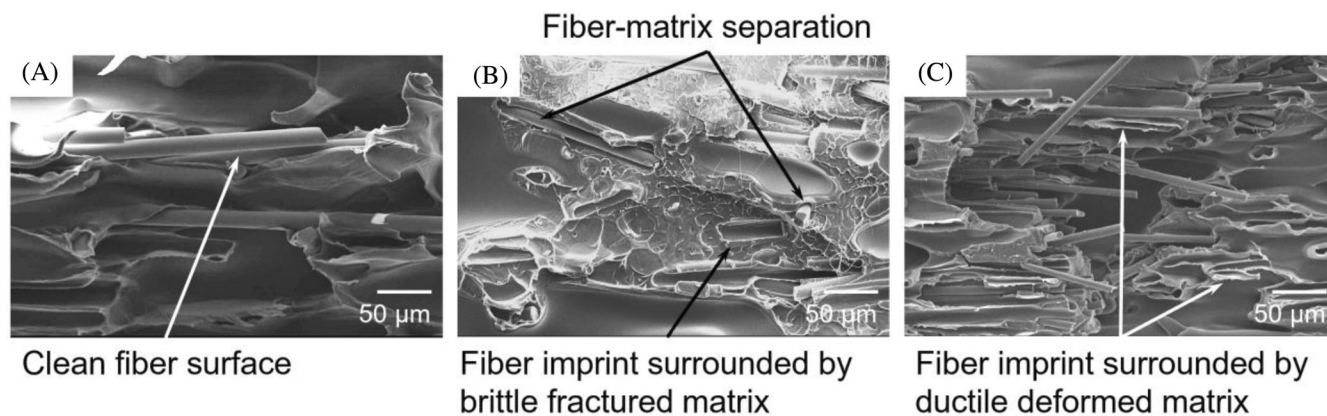
**FIGURE 7** Scanning electron microscope images of the broken surfaces in the case of (A) glass (25 w%), (B) basalt (20 w%), and (C) carbon (25 w%) fiber–reinforced composites.
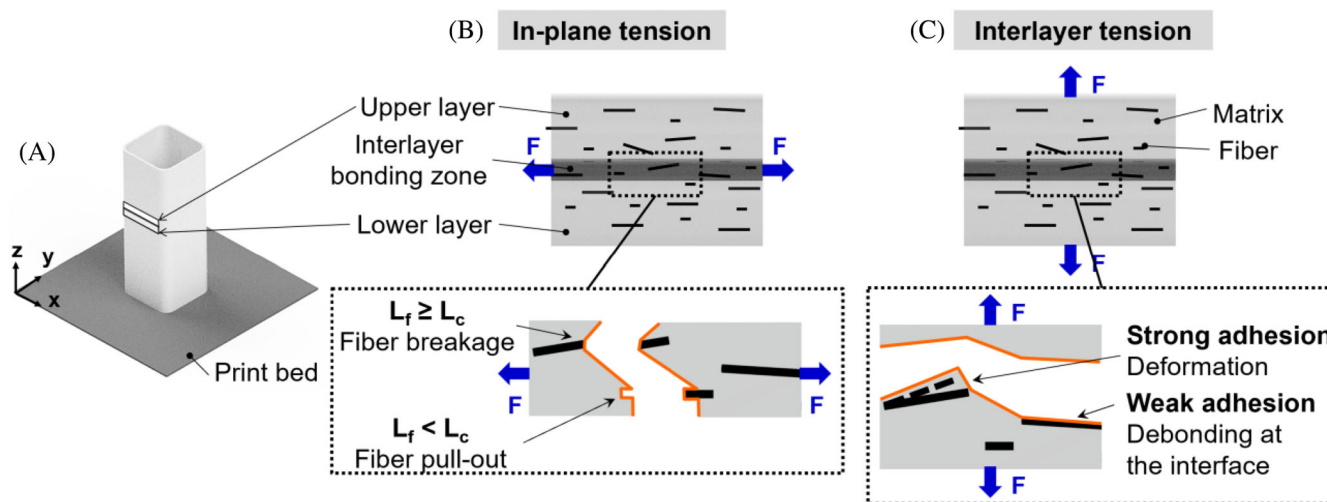


**FIGURE 8** Damage modes of short fiber–reinforced 3D-printed composites as a function of fiber–matrix adhesion quality in the case of (B) in-plane tension and (C) interlayer tension. (A) shows the interpretation of layers at macro level.

the fiber orientation is quasi parallel to the pulling direction. It should be noted that other types of stresses can lead to additional damage modes, for example, composites subjected to adhesive wear show signs of fatigue, plastic deformation and fiber thinning[7]. In this study we analyze the damage modes in terms of the fiber-matrix adhesion. If adhesion is adequate and the fiber is as long or longer than the critical fiber length, the failure is fiber breakage. In the case of poor adhesion, damage develops at the interface and the fiber pulls out. The load transfer between the fiber and the matrix is inefficient and the fiber does not reinforce the composite.

In the case of interlayer tensile tests, the force is perpendicular to the printing direction and thus to the average fiber orientation. Based on our results, we found that two different damage modes can occur, depending on the quality of fiber–matrix adhesion. In case of good adhesion, the matrix deforms, and the fibers move with it until they break or tear. Similar damage can be observed for the carbon fiber–reinforced PLA samples. If the fiber–matrix adhesion is poor, the crack runs along the interface, leading to brittle fracture and low strength. This failure mode was observed for the glass fiber composites. In the case of weak adhesion, fiber content is inversely proportional to interlayer tensile strength, since with more fiber–matrix interface, there is less area where polymer diffusion can occur between the layers.

## 4 | CONCLUSION

In this study, we investigated the in-plane and the interlayer tensile properties of glass, basalt, and carbon fiber–reinforced polylactic acid (PLA) composites. Short fiber–reinforced filaments with 5, 10, 15, 20, and 25 w% fiber content were prepared, then tensile specimens were

prepared by material extrusion 3D printing. We found that with the Halpin-Tsai model the in-plane tensile strength can be predicted with an error of less than 120%, up to 15 w% fiber content. The accuracy of prediction deteriorates for higher fiber contents as the proportion of fiber–matrix interfaces in the composite increases. Based on the in-plane tensile strength we estimated the interfacial shear strength for all composites which characterizes the quality of the adhesion between the fiber and the matrix. Interfacial shear strength was estimated to be 10.4, 7.2, and 1.4 MPa for basalt, carbon and glass, respectively. The interlayer tests showed that interlayer tensile properties are highly dependent on the quality of fiber–matrix adhesion. The estimated interfacial shear strength ($\tau$) results suggested adequate adhesion for the basalt and carbon fiber composites. Optical microscope and Scanning Electron Microscope (SEM) images showed that fibers participated in the damage process together with the matrix, and the fracture was more ductile. We found that in these cases, there is a second-order relationship between fiber content and interlayer tensile strength in the 5–25 w% range, with a maximum at 15 w%. The estimated interfacial shear strength was the lowest for the glass fiber composites. In case of the glass fiber composites, we found that fiber content is inversely proportional to interlayer tensile strength. Optical microscope and SEM images show clean fiber surfaces indicating poor adhesion. In this case the fracture runs between the fibers and the matrix. Therefore, increasing fiber content accelerates the crack propagation, leading to brittle fracture and low strength. Also, the larger the fiber-matrix interface, the smaller the area where polymer diffusion can occur between the layers, which can further degrade the interlayer properties. Our findings show that the anisotropic behavior of 3D printed composites is strongly affected by content and the quality of the fiber-matrix adhesion. In the case of inadequate adhesion, the in-plane properties improve only to a small extent with increasing fiber content, while the interlayer properties deteriorate linearly.

## ACKNOWLEDGMENTS

## DATA AVAILABILITY STATEMENT
The data that support the findings of this study are available from the corresponding author upon reasonable request.

## ORCID
*Norbert Krisztián Kovács* https://orcid.org/0000-0002-6328-8940

## REFERENCES
1. Kubota M, Hayakawa K, Todoroki A. Effect of build-up orientations and process parameters on the tensile strength of 3D printed short carbon fiber/PA-6 composites. *Adv Compos Mater.* 2022;31(2):119-136. doi:10.1080/09243046.2021.1930497
2. Dul S, Fambri L, Pegoretti A. High-performance polyamide/carbon fiber composites for fused filament fabrication: mechanical and functional performances. *J Mater Eng Perform.* 2021;30:5066-5085. doi:10.1007/s11665-02
3. Wang K, Li S, Rao Y, et al. Flexure behaviors of ABS-based composites containing carbon and Kevlar fibers by material extrusion 3D printing. *Polymers (Basel).* 2019;11(11):1878. doi:10.3390/polym11111878
4. Kariuki LW, Ikua BW, Karanja SK, Ng'ang'a SP, Zeidler H. Fused filament fabrication of carbon fiber-reinforced polymer composite: effect of process parameters on flexural properties. *Eng Rep.* 2023:e12807. doi:10.1002/eng2.12807
5. Mohankumar HR, Benal MGM, Pradeepkumar GS, et al. Effect of short glass fiber addition on flexural and impact behavior of 3D printed polymer composites. *ACS Omega.* 2023;8(10):9212-9220. doi:10.1021/acsomega.2c07227
6. de Carvalho WS, Marzemin F, Belei C, Petersmann S, Arbeiter F, Amancio-Filho ST. Statistical-based optimization of fused filament fabrication parameters for short-carbon-fiber-reinforced poly-ether-ether-ketone considering multiple loading conditions. *Polym Test.* 2023;128:108207. doi:10.1016/J.POLYMERTESTING.2023.108207
7. Yilmaz S. Comprehensive analysis of 3D printed PA6.6 and fiber-reinforced variants: revealing mechanical properties and adhesive wear behavior. *Polym Compos.* 2024;45(2):1446-1460. doi:10.1002/pc.27865
8. Wei H, Cauchy X, Navas IO, et al. Direct 3D printing of hybrid nanofiber-based nanocomposites for highly conductive and shape memory applications. *ACS Appl Mater Interfaces.* 2019;11(27):24523-24532. doi:10.1021/acsami.9b04245

9. Petrény R, Tóth C, Horváth A, Mészáros L. Development of electrically conductive hybrid composites with a poly(lactic acid) matrix, with enhanced toughness for injection molding, and material extrusion-based additive manufacturing. *Heliyon*. 2022;8(8):e10287. doi:10.1016/j.heliyon.2022.e10287

10. Soltanmohammadi K, Aberoumand M, Rahmatabadi D, et al. Four-dimensional printing of acrylonitrile butadiene styrene – thermoplastic polyurethane shape memory polymers with excellent material and interfacial adhesion performance. *Express Polym Lett*. 2023;17(11):1082-1095. doi:10.3144/expresspolymlett.2023.82

11. Pei S, Wang K, Chen CB, et al. Process-structure-property analysis of short carbon fiber reinforced polymer composite via fused filament fabrication. *J Manuf Process*. 2021;64:544-556. doi:10.1016/J.JMAPRO.2021.02.019

12. Yilmaz S. Comparative investigation of mechanical, Tribological and Thermo-mechanical properties of commonly used 3D printing materials. *European J Sci Technol*. 2022;32:827-831. doi:10.31590/ejosat.1040085

13. Ramesh M, Niranjana K. Effect of process parameters on fused filament fabrication printed composite materials. In: Praveen Kumar A, Sadasivuni KK, AlMangour B, Abdul Bin Majid MS, eds. *High-Performance Composite Structures: Additive Manufacturing and Processing*. Springer; 2022:155-178. doi:10.1007/978-981-16-7377-1_7

14. Polyzos E, Van Hemelrijck D, Pyl L. Stochastic semi-analytical modeling of reinforced filaments for additive manufacturing. *Compos Part B Eng*. 2023;262:110762. doi:10.1016/J.COMPOSITESB.2023.110762

15. Nasirov A, Gupta A, Hasanov S, Fidan I. Three-scale asymptotic homogenization of short fiber reinforced additively manufactured polymer composites. *Compos Part B Eng*. 2020;202: 108269. doi:10.1016/J.COMPOSITESB.2020.108269

16. Gupta A, Hasanov S, Fidan I, Zhang Z. Homogenized modeling approach for effective property prediction of 3D-printed short fibers reinforced polymer matrix composite material. *Int J Adv Manuf Technol*. 2022;118(11–12):4161-4178. doi:10.1007/s00170-021-08230-9

17. Abderrafai Y, Hadi Mahdavi M, Sosa-Rey F, et al. Additive manufacturing of short carbon fiber-reinforced polyamide composites by fused filament fabrication: formulation, manufacturing and characterization. *Mater Des*. 2022;214:110358. doi:10.1016/J.MATDES.2021.110358

18. Alipour A, Lin R, Jayaraman K. Enhancement of performance in flax/epoxy composites by developing interfacial adhesion using graphene oxide. *Express Polym Lett*. 2023;17(5):471-486. doi:10.3144/expresspolymlett.2023.35

19. Yu S, Hwang YH, Lee KT, Kim SO, Hwang JY, Hong SH. Outstanding strengthening and toughening behavior of 3D-printed fiber-reinforced composites designed by biomimetic interfacial heterogeneity. *Adv Sci*. 2022;9(3):2103561. doi:10.1002/advs.202103561

20. Yilmaz S, Gul O, Eyri B, Karsli NG, Yilmaz T. Analyzing the influence of multimaterial 3D printing and Postprocessing on mechanical and Tribological characteristics. *Macromol Mater Eng*. 2024;309:2300428. doi:10.1002/mame.202300428

21. Ramesh M, Rajeshkumar L, Balaji D. Influence of process parameters on the properties of additively manufactured fiber-reinforced polymer composite materials: a review. *J Mater Eng Perform*. 2021;30(7):4792-4807. doi:10.1007/s11665-021-05832-y

22. König M, Diekmann J, Lahres M, Middendorf P. Experimental investigation of process-structure effects on interfacial bonding strength of a short carbon fiber/polyamide composite fabricated by fused filament fabrication. *Prog Addit Manuf*. 2022; 7(4):593-607. doi:10.1007/s40964-021-00249-4

23. Bhandari S, Lopez-Anido RA, Gardner DJ. Enhancing the interlayer tensile strength of 3D printed short carbon fiber reinforced PETG and PLA composites via annealing. *Addit Manuf*. 2019;30:100922. doi:10.1016/J.ADDMA.2019.100922

24. Zotti A, Zuppolini S, Tábi T, et al. Effects of 1D and 2D nanofillers in basalt/poly(lactic acid) composites for additive manufacturing. *Compos Part B Eng*. 2018;153:364-375. doi:10.1016/J.COMPOSITESB.2018.08.128

25. Binaz V, Deepak K, Singh I. Comparative assessment of cutting processes in the mechanical behavior of basalt fiber/poly(lactic acid) matrix composites. *Express Polym Lett*. 2023;17(2):152-168. doi:10.3144/expresspolymlett.2023.11

26. Tóth C, Kovács NK. Comparison of the accuracy of analytical models for basalt fiber–reinforced poly(lactic acid) composites prepared by injection molding and fused filament fabrication. *Int J Adv Manuf Technol*. 2022;121(5–6):3999-4010. doi:10.1007/s00170-022-09572-8

27. Handermann A, Llc B, Whitepaper Z. Oxidized Polyacrylonitrile fiber properties, products and applications. 2017 https://www.researchgate.net/publication/298614209

28. Camarena E, Clarke RJ, Ennis BL. Development of a compressive failure model for carbon fiber composites and associated uncertainties. *Compos Sci Technol*. 2021;211:108855. doi:10.1016/J.COMPSCITECH.2021.108855

29. Fu SY, Lauke B, Mäder E, Yue CY, Hu X. Tensile properties of short-glass-fiber- and short-carbon-fiber-reinforced polypropylene composites. *Compos Part A Appl Sci Manuf*. 2000;31(10): 1117-1125. doi:10.1016/S1359-835X(00)00068-3

30. Tábi T, Gere D, Csézi G, Pölöskei K. Influence of Epoxidized natural rubber of the thermoformability of poly(lactic acid) biopolymer films using elevated temperature ball burst tests. *J Therm Anal Calorim*. 2024;149(1):75-87. doi:10.1007/s10973-023-12712-1

31. Fallon JJ, McKnight SH, Bortner MJ. Highly loaded fiber filled polymers for material extrusion: a review of current understanding. *Addit Manuf*. 2019;30:100810. doi:10.1016/J.ADDMA.2019.100810

32. Fu SY, Lauke B, Mai YW. Major factors affecting the performance of short fibre reinforced polymers. *Sci Eng Short Fibre Reinf Polym Compos*. 2009;1:29-58. doi:10.1533/9781845696498.29

33. Yan J, Demirci E, Gleadall A. Are classical fibre composite models appropriate for material extrusion additive manufacturing? A thorough evaluation of analytical models. *Addit Manuf*. 2023;62:103371. doi:10.1016/J.ADDMA.2022.103371

34. Shafighfard T, Cender TA, Demir E. Additive manufacturing of compliance optimized variable stiffness composites through short fiber alignment along curvilinear paths. *Addit Manuf*. 2021;37:101728. doi:10.1016/J.ADDMA.2020.101728

35. Yang D, Zhang H, Wu J, McCarthy ED. Fibre flow and void formation in 3D printing of short-fibre reinforced thermoplastic composites: An experimental benchmark exercise. *Addit Manuf*. 2021;37:101686. doi:10.1016/J.ADDMA.2020.101686

36. Sang L, Han S, Peng X, Jian X, Wang J. Development of 3D-printed basalt fiber reinforced thermoplastic honeycombs with

enhanced compressive mechanical properties. *Compos Part A Appl Sci Manuf*. 2019;125:105518. doi:10.1016/J.COMPOSITESA.2019.105518

37. Coughlin N, Drake B, Fjerstad M, et al. Development and mechanical properties of basalt fiber-reinforced acrylonitrile butadiene styrene for in-space manufacturing applications. *J Compos Sci*. 2019;3(3):89. doi:10.3390/jcs3030089

38. Tekinalp HL, Kunc V, Velez-Garcia GM, et al. Highly oriented carbon fiber–polymer composites via additive manufacturing. *Compos Sci Technol*. 2014;105:144-150. doi:10.1016/J.COMPSCITECH.2014.10.009

39. Yu S, Hwang YH, Hwang JY, Hong SH. Analytical study on the 3D-printed structure and mechanical properties of basalt fiber-reinforced PLA composites using X-ray microscopy. *Compos Sci Technol*. 2019;175:18-27. doi:10.1016/J.COMPSCITECH.2019.03.005

40. Kim Y, Park OO. Effect of fiber length on mechanical properties of injection molded long-fiber-reinforced thermoplastics. *Macromol Res*. 2020;28(5):433-444. doi:10.1007/s13233-020-8056-6

41. Yan X, Cao S. Structure and interfacial shear strength of polypropylene-glass fiber/carbon fiber hybrid composites fabricated by direct fiber feeding injection molding. *Compos Struct*. 2018;185:362-372. doi:10.1016/J.COMPSTRUCT.2017.11.037

42. Zhang H, Zhang L, Zhang H, Wu J, An X, Yang D. Fibre bridging and nozzle clogging in 3D printing of discontinuous carbon fibre-reinforced polymer composites: coupled CFD-DEM modelling. doi:10.1007/s00170-021-07913-7/Published

43. Hou X, Yao S, Wang Z, Fang C, Li T. Enhancement of the mechanical properties of polylactic acid/basalt fiber composites via in-situ assembling silica nanospheres on the interface. *J Mater Sci Technol*. 2021;84:182-190. doi:10.1016/J.JMST.2021.02.001

44. Ying Z, Wu D, Zhang M, Qiu Y. Polylactide/basalt fiber composites with tailorable mechanical properties: effect of surface treatment of fibers and annealing. *Compos Struct*. 2017;176:1020-1027. doi:10.1016/J.COMPSTRUCT.2017.06.042

45. Li H, Wang T, Joshi S, Yu Z. The quantitative analysis of tensile strength of additively manufactured continuous carbon fiber reinforced polylactic acid (PLA). *Rapid Prototyp J*. 2019;25(10):1624-1636. doi:10.1108/RPJ-01-2018-0005

46. Chen R, Misra M, Mohanty AK. Injection-moulded biocomposites from polylactic acid (PLA) and recycled carbon fibre: evaluation of mechanical and thermal properties. *J Thermoplast Compos Mater*. 2014;27(9):1286-1300. doi:10.1177/0892705712471360

47. Consul P, Beuerlein KU, Luzha G, Drechsler K. Effect of extrusion parameters on short fiber alignment in fused filament fabrication. *Polymers (Basel)*. 2021;13(15):2443. doi:10.3390/polym13152443

48. Yan J, Demirci E, Ganesan A, Gleadall A. Extrusion width critically affects fibre orientation in short fibre reinforced material extrusion additive manufacturing. *Addit Manuf*. 2022;49:102496. doi:10.1016/J.ADDMA.2021.102496

49. Hanhan I, Sangid MD. Damage propagation in short fiber thermoplastic composites analyzed through coupled 3D experiments and simulations. *Compos Part B Eng*. 2021;218:108931. doi:10.1016/J.COMPOSITESB.2021.108931

50. Mészáros L, Horváth A, Vas LM, Petrény R. Investigation of the correlations between the microstructure and the tensile properties multi-scale composites with a polylactic acid matrix, reinforced with carbon nanotubes and carbon fibers, with the use of the fiber bundle cell theory. *Compos Sci Technol*. 2023;242:110154. doi:10.1016/J.COMPSCITECH.2023.110154